Earth and Planetary Science Letters 584 (2022) 117473

Contents lists available at ScienceDirect

Earth and Planetary Science Letters

www.elsevier.com/locate/epsl

Structural evolution in a pyrolitic magma ocean under mantle conditions

Dongyang Huang [a,*], Motohiko Murakami [a], John Brodholt [b], Catherine McCammon [c], Sylvain Petitgirard [a]

[a] Institute of Geochemistry and Petrology, ETH Zürich, 8092 Zürich, Switzerland
[b] Department of Earth Sciences, University College London, London, UK
[c] Bayerisches Geoinstitut, University of Bayreuth, D-95440 Bayreuth, Germany

ARTICLE INFO

Article history:
Received 12 October 2021
Received in revised form 13 February 2022
Accepted 23 February 2022
Available online 7 March 2022
Editor: R. Dasgupta

Keywords:
magma ocean
silicate melt structure
acoustic velocity
ab initio
diamond anvil cell
early Earth's interior

ABSTRACT

Structure and properties of terrestrial magma oceans control the co-evolution of the core, mantle and atmosphere of the early Earth, but are poorly understood because discrepancies remain between experiments and theoretical calculations. Here we combine acoustic velocity measurements and ab initio simulations on pyrolite glass/melt with a silicate Earth-like composition. In the complex system, we find a gradual increase of sound velocity with increasing pressure. Through ab initio simulations, this is explicable by the transition from four- to six-fold coordinated Si occurring over the entire mantle regime. These results are at odds with recent X-ray diffraction measurements, which show an abrupt change in Si-O coordination at 35 GPa. It is however consistent with recent high-pressure data, where Ni partitioning between molten metal and silicate exhibits a similar gradual change with pressure. Unlike amorphous silica, smooth structural evolution in a multicomponent system implies progressive changes in magma ocean properties with depth, such as density, element partitioning and transport properties, which, when incorporated into magma ocean models, may improve our understanding of early history of the Earth and other rocky planets.

1. Introduction

Magma oceans are expected on terrestrial planets during early accretion processes, as a result of substantial heating contributed mainly by the release of kinetic and potential energy during stochastic impacts and core segregation (e.g. (Elkins-Tanton, 2012; Solomatov, 2015)). The fate of molten silicates that form magma oceans is determined by their structures at varying depths, because melt structure controls key properties, such as density and transport properties (diffusivity, viscosity and thermal conductivity) that govern the mobility of magma (depending on density and viscosity at depth) and thermal history of early planets. For a differentiated body like the Earth, pressure-induced melt structure change is particularly essential as it affects element partitioning between iron-rich metal and silicate (core-mantle differentiation) in a deep magma ocean (Keppler and Rubie, 1993).

A key structural property of silicate melts is the coordination of cations forming the basic units (cation-oxygen polyhedra) of silicate network; these cations are thus termed network formers and mainly include Si^{4+} and Al^{3+} (by charge balance) (Mysen, 1983). Because probing such structure in melts is extremely challenging under simultaneously high P-T conditions, to date only one study reported in situ structural data on a molten silicate (basalt) up to 60 GPa (Sanloup et al., 2013). Alternatively, as an analogue, glass has been widely used to investigate structure and density changes of silicate melts with pressure, including geophysically important end-member systems, that is SiO_2 (e.g. (Murakami and Bass, 2010; Sato and Funamori, 2010; Petitgirard et al., 2017; Prescher et al., 2017; Petitgirard et al., 2019; Kono et al., 2020)), $MgSiO_3$ (e.g. (Lee et al., 2008; Murakami and Bass, 2011; Petitgirard et al., 2015; Kono et al., 2018)), whereas multicomponent compositions pertinent to terrestrial magma oceans have yet been explored. On the other hand, based on fundamentals of quantum mechanics, recent molecular dynamics simulations have greatly expanded our understanding of silicate melts by predicting their structural variations in a much larger P-T-composition space (Stixrude and Karki, 2005; Karki et al., 2007; Bajgain et al., 2015), which however demands further experimental validation. As regards the transition pressure of Si-O coordination from four-fold to six-fold, excel-

* Corresponding author.
E-mail address: dongyang.huang@erdw.ethz.ch (D. Huang).

https://doi.org/10.1016/j.epsl.2022.117473

lent agreement has been achieved in SiO_2 (45±10 GPa (Karki et al., 2007; Benmore et al., 2010; Sato and Funamori, 2010; Murakami and Bass, 2010; Prescher et al., 2017; Petitgirard et al., 2019; Kono et al., 2020)) and $MgSiO_3$ (125-135 GPa (Stixrude and Karki, 2005; Murakami and Bass, 2011)) among X-ray diffraction results, sound velocity measurements and theoretical predictions. However, in more complex basaltic melts, major discrepancies remain between high-pressure X-ray diffraction data and ab initio calculations. For instance, similar to SiO_2, the experiments found that the 4 to 6 coordination transition was completed at ~35 GPa (Sanloup et al., 2013), whereas ab initio results suggest that some lower-coordinate Si persists until ~120 GPa (Bajgain et al., 2015).

Composition is the intrinsic factor that determines the structure and properties of magma oceans, given a certain pressure-temperature condition. For decades, SiO_2 (and more recently $MgSiO_3$) glass has been studied under mantle conditions not only as an analogue to melt, but also as a basis for multicomponent systems, because of its compositional simplicity. And indeed as discussed above, convergence emerges from different techniques in these simple systems. However, difficulties encountered in the more complex system render experimenting on a realistic composition, instead of extrapolation, necessary. Here, we respectively performed in situ Brillouin scattering measurements and ab initio molecular dynamics simulations on pyrolite glass and melt, a model composition representative of the bulk silicate Earth. Over the entire mantle pressure range, the acoustic wave velocity changes continuously, corroborating the predicted smooth structural modifications. Unlike abrupt and rapid structural changes in highly polymerized SiO_2 glass/melt at depth, nor like instantaneous phase transitions in minerals that mark the discontinuities in the present-day mantle, gradual densification and coordination increase are expected in multicomponent terrestrial magma oceans.

2. Methods

2.1. Sample preparation

The starting silicate glass was modeled after the composition of pyrolite (McDonough and Sun, 1995), by mixing and grinding high purity (≥99%) oxides and carbonate powders (FeO, MgO, Al_2O_3, SiO_2 and $CaCO_3$) under ethanol in an agate mortar (Table 1). The powder mixture was firstly decarbonated at 950 °C for 12 h and then compressed into a pellet, which was further fused into a glass bead by aerodynamic levitation coupled with a 75 W CO_2 laser (λ = 10.6 μm). Before quenched into glass, the pellet was equilibrated with a CO_2-H_2 gas mixture (10:90, diluted with an Ar carrier gas) for ~30 s, at 1900 °C and 1 bar. The redox equilibrium between molten pellet and the gas mixture imposed the fO_2 at ΔIW-1.2 (oxygen fugacity in log units relative to the iron-wüstite buffer). Chemical homogeneity of the silicate glass was confirmed by wavelength dispersive X-ray spectroscopy (WDS) using electron probe micro-analysis (EPMA) on a JEOL JXA-8230 at ETH. A beam energy of 15 keV and a current of 20 nA were used throughout. The standards used were albite for Si, synthetic forsterite for Mg, anorthite for Ca, Al, and synthetic fayalite for Fe. All elements were analyzed using K_α line. Oxygen was calculated by cation stoichiometry. Results were the average of 12 points and detection limits ranged from 50-90 ppm for all elements. Mössbauer spectroscopy determined at BGI found no evidence for ferric iron in the glass (Fig. S1), with a detection limit estimated to be 0.05, i.e. $Fe^{3+}/\sum Fe$ = 0.00±0.05. At the vicinity of the proposed pressure (~70 GPa) for spin crossover in ferrous iron (Nomura et al., 2011), no anomaly was observed in the velocity data (Table 3 and Fig. 2), which is consistent with a recent study on basaltic glass (Maeda et al., 2017). High pressure was generated using a symmetric diamond anvil cell (DAC). A Re gasket was pre-indented to 25-30 μm thick by diamond anvils with flat culet diameters of 120 μm beveled at 10° up to 300 μm. The pyrolite glass was crushed in a rock crusher, and shards were loaded into a 70 μm hole drilled in the Re gasket without pressure-transmitting medium. As an indicator of stress conditions inside the sample chamber, the full width at half maximum (FWHM) of the Brillouin peak is reported in Table 3. As can be seen in Fig. S2, there is no systematic broadening of the peaks under higher pressure conditions, indicating insignificant increase of deviatoric stress with pressure.

Table 1
EPMA results for the silicate glass, compared with pyrolite and KLB-1 peridotite (major components only). Values in parenthesis are 1 standard deviations.

wt%	Glass (This work)	Pyrolite (McDonough and Sun, 1995)	KLB-1 peridotite (Takahashi, 1986)
SiO_2	47.17(14)	45.00	44.48
Al_2O_3	4.60(4)	4.45	3.59
FeO(t)	8.09(5)	8.05	8.10
MgO	38.34(11)	37.80	39.22
CaO	2.33(2)	3.55	3.44
Total	100.54(16)	98.85	98.83

2.2. Sound velocity measurements by Brillouin spectroscopy

In situ high-pressure Brillouin scattering measurements of sound velocities were performed in the symmetric DAC at room temperature. The pyrolite glass under pressure was probed by a diode-pumped solid-state laser with a wavelength of 532 nm (Verdi V6, Coherent). The size of the incident laser beam focused on the sample was ~10 μm in diameter. Forward symmetric geometry with a 50° external scattering angle was used in all measurements. A borosilicate crown glass (BK7) was used as a standard material to calibrate the scattering angle. The scattered light passed through a six-pass tandem Fabry-Pérot interferometer and was measured by a multichannel analyzer (GHOST v.6.75, JRS Scientific Instruments). The spectrum of the scattered light contains a central unshifted line, corresponding to Rayleigh scattering, and Brillouin-scattered Stokes and anti-Stokes lines, which were produced by inelastic scattering of acoustic phonons. The symmetric scattering geometry allows one to calculate the velocity V_i of an acoustic wave without knowing the refractive index of the sample by

$$V_i = \Delta\omega_i \lambda / 2sin(\frac{\theta}{2}), \quad (1)$$

where $\Delta\omega_i$ is the Brillouin frequency shift of a given acoustic mode i, λ the incident laser wavelength (532 nm) and θ the external scattering angle (50°). In total 31 Brillouin spectra were collected at different, occasionally nearly identical pressures from 30 to 157 GPa, in two independent runs (Table 3). The overlapping of velocities at similar pressures from the two runs demonstrates the reproducibility of current measurements. For a Brillouin spectrum with sufficiently high signal-to-noise ratio, the acquisition time required generally increases with pressure, which turned out to be from 2 to 20 h. Pressure was determined before and after each Brillouin measurement, using the high frequency edge of diamond's Raman shift (Akahama and Kawamura, 2004). Note that a relatively small but systematic pressure increase by ~3 GPa was observed after each Brillouin measurement, compared to the value determined before; pressure was thus reported as the mean of both. At each pressure, the raw Brillouin spectrum was fitted with Gaussian function to determine peak positions of Stokes and anti-Stokes lines, whose average was used to obtain $\Delta\omega_i$. Pressure hysteresis is a well-known phenomenon during decompression (e.g.

Table 2
Pyrolite supercell containing 151 atoms. Elemental abundances are given in number of atoms and wt%, and are compared with the pyrolite model by McDonough and Sun (1995). Core radii, number of valence electrons treated by the pseudopotentials, and Bader charge are also shown.

Elements	Z	Number	wt%	Pyrolite model (wt%)	Radius (Bohr)	Radius (Å)	Valence electrons	Bader charge
O	8	88	44.5	44	1.52	0.80	6	−1.53
Mg	12	30	23.0	22.8	2	1.06	8	1.70
Al	13	3	2.4	2.35	1.9	1.01	3	2.27
Si	14	24	21.2	21	1.9	1.01	4	2.93
Ca	20	2	2.6	2.53	3	1.59	8	1.52
Fe	26	4	6.3	6.26	2.2	1.16	14	0.89

Table 3
Transverse wave velocity (Vs) and full width at half maximum (FWHM) of Brillouin peak from TA mode of the pyrolite glass at different pressures (P). Errors are 1 sigmas.

P (GPa)	error (GPa)	Vs (km/s)	error (km/s)	FWHM (GHz)	error (GHz)
30.04	2.68	4.57	0.04	0.44	0.01
36.68	1.07	4.70	0.04	0.54	0.03
41.02	1.53	4.82	0.03	0.58	0.04
46.69	1.96	4.98	0.02	0.51	0.03
55.36*	1.62	5.14	0.01	0.46	0.00
56.30	2.19	5.14	0.04	0.47	0.07
61.74	1.63	5.19	0.02	0.56	0.05
62.42*	2.57	5.20	0.02	0.44	0.04
68.48	3.41	5.28	0.03	0.63	0.04
69.42*	2.14	5.30	0.02	0.50	0.04
75.36*	1.93	5.38	0.02	0.43	0.03
79.85*	1.71	5.43	0.02	0.42	0.03
84.94	2.37	5.46	0.03	0.60	0.00
88.29	0.29	5.50	0.04	0.66	0.19
91.10	0.87	5.56	0.04	0.46	0.05
93.28	0.59	5.58	0.04	0.66	0.12
96.04	1.57	5.61	0.02	0.58	0.06
99.81	0.50	5.74	0.00	0.61	0.08
103.66	0.87	5.74	0.03	0.58	0.13
107.77	1.15	5.80	0.02	0.52	0.06
111.94	0.94	5.81	0.02	1.00	0.64
117.79	1.65	5.85	0.02	0.49	0.13
122.92	0.99	5.89	0.03	0.45	0.10
127.72	1.12	5.94	0.03	0.53	0.10
131.15	0.77	5.95	0.02	0.53	0.19
135.59	0.81	5.97	0.00	0.52	0.05
139.17	0.83	5.98	0.02	0.45	0.09
142.46	0.43	5.96	0.02	0.43	0.11
147.28	0.82	6.00	0.00	0.44	0.12
152.83	0.87	6.06	0.03	0.47	0.10
157.36	0.88	6.03	0.00	0.46	0.02

Note: ∗ denotes measurement from different loading.

(Sanchez-Valle and Bass, 2010)), however we were unable to obtain decompression data because the diamonds ineluctably broke at very high pressures. Nonetheless, this does not affect the application of the velocity results to inferring structural evolution in a convecting magma ocean (thus involving both compression and decompression): the high diffusivity and low viscosity (Karki and Stixrude, 2010) of silicate melts at high temperatures (thousands of degrees) in the magma ocean are expected to counterbalance to some extent the pressure hysteresis observed in solids during high pressure experiments.

2.3. Ab initio molecular dynamics simulations

We conducted ab initio simulations using Vienna Ab initio Simulation Package (Kresse and Hafner, 1993) based on the projector augmented wave (PAW) method (Blöchl, 1994; Kresse and Joubert, 1999). The exchange-correlation functionals were treated using the generalized gradient approximation (GGA) in the Perdew–Burke–Ernzerhof (PBE) form (Perdew et al., 1996). A supercell consists of 151 atoms ($Fe_4Mg_{30}Si_{24}Ca_2Al_3O_{88}$) was designed according to the same pyrolitic composition (McDonough and Sun, 1995) to approximate the average magma ocean. Valence configurations and the core radii for each element are listed in Table 2. All calculations were non-spin-polarized. In line with previous non-spin-polarized simulations in basaltic melts (Bajgain et al., 2015), for iron we obtained slightly smaller ionic radius, and thus less coordination (Fig. 3), relative to the spin-polarized silicate melt (Solomatova and Caracas, 2019). As for the high-to-low spin transition in iron, it has been shown previously that full spin transition does not occur at possible P-T conditions of the magma ocean (Caracas et al., 2019). The gamma point was used to sample the Brillouin zone, with 500 eV cutoff energy for the plane wave expansion. Convergence test was performed with denser (2*2*2) k-point grid; with higher cutoff energy (900 eV), the Pulay stress was found to be less than 0.6 GPa. Atoms were initially randomly distributed and heated at 6000 K for at least 8 ps to obtain silicate melt structure before being equilibrated at 4000 K from 10 to 148 GPa. The canonical ensemble (NVT) was used with a Nosé-Poincaré thermostat to control the temperature. Simulations were run for 13-30 ps with a time step of 1 femtosecond (fs) with the first 1 ps being discarded. P and T were calculated from the time average. Details for data processing are given in SI.

3. Results

3.1. Sound velocity in pyrolite glass

Over the entire investigated pressure range, well-defined peaks from transverse acoustic waves are constantly observed. With increasing pressure, Stokes and anti-Stokes lines of pyrolite's transverse acoustic modes shift away from the central Rayleigh line (Fig. 1). The longitudinal modes of the glass with larger frequency shifts are blocked by transverse acoustic modes of the diamond anvils in all measurements. Transverse wave velocities (Vs) calculated from Eq. (1) are plotted in Fig. 2 as a function of pressure. As a result of the sharp peaks exemplified in Fig. 1, the uncertainties on Vs are found to be 0.4% on average (Table 3). All the data from 30 to 157 GPa can be fitted with a quadratic polynomial function ($R^2 = 0.995$, solid curve in Fig. 2). Residual analysis (Fig. S3) further confirms the robustness of the quadratic fit over the entire investigated pressure range. Sharp changes in transverse wave velocity observed in solid Earth are associated with first-order phase transitions in minerals (Birch, 1952). The lack of such changes in our velocity data thus indicates that structural modifications in pyrolite glass take place rather smoothly up to 157 GPa. This becomes clearer when one compares the Vs-P trend of pyrolite with those of silica and $MgSiO_3$ glasses (Murakami and Bass, 2010, 2011), which exhibit discontinuous changes at ∼40 GPa in silica and at 133 GPa in $MgSiO_3$ (as indicated by downwards arrows in Fig. 2, see discussions below). The sound velocity evolution indicates gradual changes of vibrational energy (phonons) in pyrolite glass with pressure, which provides important insight into the pressure-induced densification process, but indirect evidence for

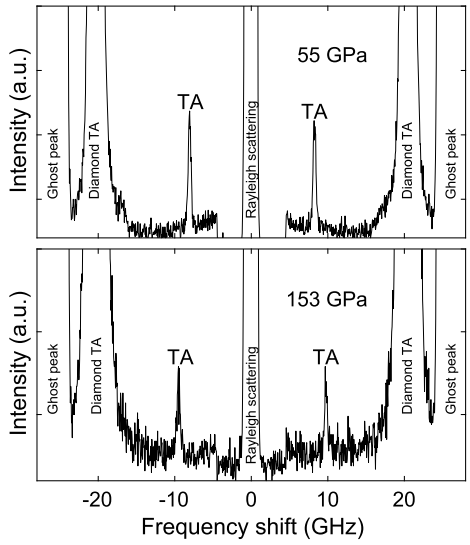

Fig. 1. Brillouin spectra of pyrolite glass. TA denotes transverse acoustic mode of the Brillouin shift. Ghost peaks are artefacts of the interferometry method.

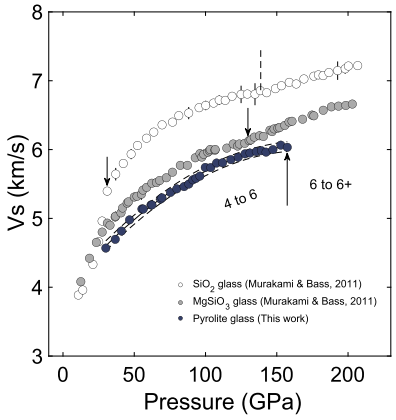

Fig. 2. Transverse acoustic wave velocities Vs of SiO_2, $MgSiO_3$ and pyrolite glass. SiO_2 (white dots) and $MgSiO_3$ (gray dots) are taken from previous studies (Murakami and Bass, 2010, 2011). Number denotes the inferred Si-O coordination under relevant pressure range. Solid curve represents the quadratic fit, while the dashed curves denote the estimated 95% prediction interval. Arrows indicate the approximate pressures where the transitions of Si coordination from four-fold to six-fold are thought to complete, which negatively correlate with the degree of polymerization in silicate glasses (see text for details). The vertical dashed line shows the potential onset of higher Si-O coordination in silica (Murakami and Bass, 2010). The upwards arrow for pyrolite glass only indicates the lower pressure bound for any possible higher Si coordination (see text for details). Error bars (1σ) are shown when larger than symbols.

microscopic structural changes. In this regard, molecular dynamics simulations are able to provide complementary and supporting information on structural variations.

3.2. Melt structure in molten pyrolite

Bond lengths obtained from our ab initio molecular dynamics simulations show that densification with increasing pressure primarily occurs via the bond shortening between the most abundant species in pyrolite melt, that is oxygen (see O-O bond lengths in Fig. 3 and Table S1), consistent with previous theoretical and experimental studies on simpler silicate melt/glass (Karki et al., 2007; Kim et al., 2019). It can be seen that, P and T being equal, higher coordination generally corresponds to larger bond length; for instance, Mg-O coordination (eightfold) is higher than that of Si-O (sixfold) at 131 GPa (Fig. 3). Nevertheless, exception (e.g. Fe-O) exists to this trend, due to the interplay of ionic radius, coordination number and spin state (see Methods) under different P-T conditions. Bond length changes in cation-oxygen pairs are rather limited as a function of pressure, if not unresolvable. Ca-O bond distances gently decrease from 2.28 Å to 2.12 Å with increasing pressure, whereas Mg-O, Fe-O and Al-O bond lengths slightly increase at first because their coordination numbers (and thus the polyhedra sizes) increase more rapidly at lower pressures. In agreement with previous simulations (Karki et al., 2007; Solomatova and Caracas, 2019), Si-O bond lengths remain relatively constant between 1.63 Å and 1.64 Å.

The densification process is also accompanied by increases of coordination for all cations, but a decrease for O-O coordination; the latter results from the significant shortening of O-O bond. Note that the average coordination number of O around O invariably decreases with pressure (Fig. 3 and details in Fig. S5), instead of becoming stabilized at 12 (icosahedron) as observed by force-field molecular dynamics simulations (Spera et al., 2011). The coordination numbers of Ca, Fe and Al with respect to O are more scattered than those of Si and Mg, which is a shared feature with previous ab initio supercells (e.g. (Solomatova and Caracas, 2019)), due to low numbers of these atoms (2 Ca, 3 Al and 4 Fe atoms in our 151-atom supercell). In previous simulations on basaltic melts, which simulated with sufficient amount of Ca, Fe and Al atoms, the coordination of these elements shows continuous changes with pressure (Bajgain et al., 2015). Therefore, the scattering of Ca, Fe and Al coordination does not necessarily undermine the conclusion of smooth structural changes in pyrolitic melt; it is simply due to insufficient resolution for low-abundance elements in our simulations. This is further corroborated by the smooth increase observed for Si and Mg coordination (Fig. 3), because of their high abundances (24 and 30 atoms, respectively; Table 2).

As a basic structural unit forming the silicate network, the Si-O coordination is particularly relevant to magma ocean properties, and is expected to increase with pressure. Due to the competition between the increasing sixfold and the persistent fivefold Si-O coordination with pressure, earlier ab initio studies on basaltic melts coincided in that the mean Si-O coordination remains less than 6 at pressures below 120 GPa (Bajgain et al., 2015; Majumdar et al., 2020; Feng et al., 2021). This however contrasts with X-ray diffraction results that proposed a much lower 4-to-6 transition pressure (35 GPa) in molten basalt (Sanloup et al., 2013). On the other hand, our detailed speciation analysis (Fig. S6) shows that SiO_6 is the dominant species (70%), with similar and small fractions of SiO_5 and SiO_7 (both ~15%), leading to an average coordination of 6 at 131 GPa and 4000 K. This is in agreement with earlier simulations on pyrolite melt, where they found (i) ~80% SiO_6, ~10% for both SiO_5 and SiO_7 at 150 GPa 4000 K, and (ii) an average coordination of 6 at 140-160 GPa and 3000-5000 K (Solomatova and Caracas, 2019). Together with the continuous increase of Si-O coordination from 4 to 6 up to 131 GPa (Fig. 3), these findings are in line with the smooth velocity change observed in pyrolite glass up to 157 GPa (Fig. 2). It is possible that Si-O coordination further increases to beyond 6 at higher pressures, however the exact pressure required for higher Si-O coordination to occur cannot be obtained from the current dataset, because there are no such changes in the velocity trend of pyrolite within the investigated pressure interval (30 to 157 GPa) as those found in SiO_2 and $MgSiO_3$ glasses. Consequently, the upwards arrow at 157 GPa in Fig. 2 indicates the lower bound for the transition to higher Si-O coordination in pyrolite glass, if it happens at all.

This is distinct from the proposed transition pressures in SiO_2 and $MgSiO_3$ glasses. As mentioned earlier, in SiO_2 glass, Si-O coordination transition from 4 to 6 has generally been determined to complete at 45±10 GPa, based on X-ray diffraction/scattering results (Benmore et al., 2010; Sato and Funamori, 2010; Prescher

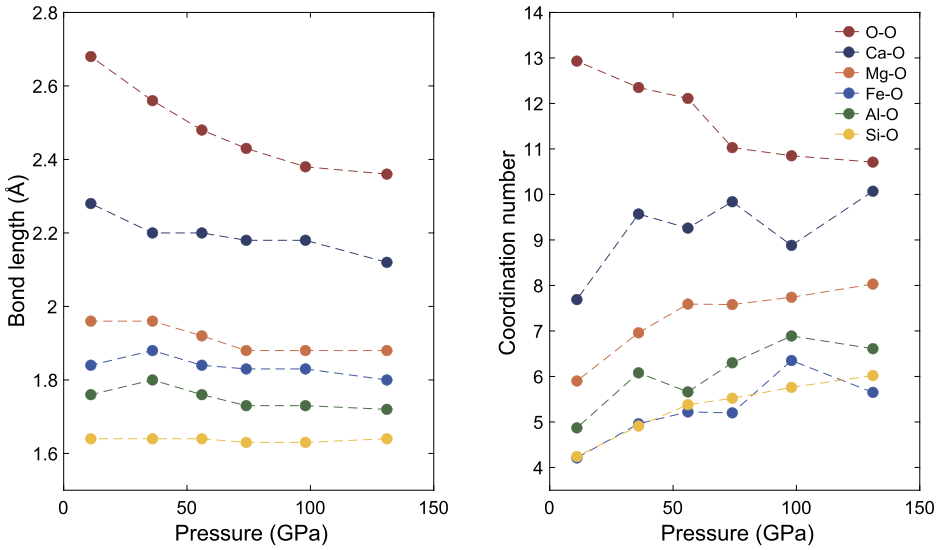

Fig. 3. Bond length and average coordination number of cation-O in pyrolite melt at 4000 K from ab initio simulations. Cation-O bond lengths exhibit relatively limited variations with pressure, compared to the significant O-O bond shortening. As a result, O-O coordination decreases from ∼13 at 11 GPa to ∼11 at 131 GPa, whereas coordination of all the cations generally increases with pressure. Zigzag curves for Ca-O, Fe-O, Al-O coordination are due to low abundances of these cations in the pyrolitic supercell (Table 2). In particular, Si-O coordination gradually increases from 4 to 6 over the entire mantle regime.

et al., 2017; Petitgirard et al., 2019; Kono et al., 2020), in agreement with both calculations and sound velocity measurements (Karki et al., 2007; Murakami and Bass, 2010). In less polymerized $MgSiO_3$ glass, the transition is predicted to finish at 125-135 GPa, as found by the two independent techniques (Stixrude and Karki, 2005; Murakami and Bass, 2011). This was further supported by recent density measurements on glasses (Petitgirard et al., 2015, 2017), where the kink in the density profile of SiO_2 and the absence of such kink in that of $MgSiO_3$ coincide with the observed composition-dependent structural changes. Note that the agreement between simulated hot and experimented cold amorphous silicates seems to render the effect of temperature negligible.

The upwardly adjusted transition pressure with increasingly complex system can be explained by the degree of polymerization in silicates. With increasing pressure, as the silicate becomes denser via bonding rearrangements, network modifiers (Mg, Fe, Ca in pyrolite) would compete for O because their own coordination numbers are bound to increase as well (Fig. 3). As a consequence, the transition to six-fold Si-O coordination would be more prolonged with increasing content of network modifiers. Known by both force field- and density functional theory-based molecular dynamics simulations (including this study), this interpretation is however in contrast to synchrotron X-ray diffraction measurements on molten basalt (containing ∼30 wt% network-modifiers) (Sanloup et al., 2013), which found its transition pressure from 4- to 6-fold coordinated Si to be the same as silica. Our pyrolite glass contains ∼51 wt% network-modifying oxides (Table 1), the most depolymerized silicate shown in Fig. 2, which explains the extended pressure range required by its gradual structural modifications.

4. Discussion

Another argument that substantiates the uninterrupted structural evolution in pyrolite glass comes from siderophile element partitioning. Because of its highly pressure-sensitive nature, Ni partitioning between molten metal and silicate has been used to constrain pressure conditions during core formation in the magma ocean (Li and Agee, 1996; Bouhifd and Jephcoat, 2011; Siebert et al., 2012; Badro et al., 2015; Fischer et al., 2015; Huang et al., 2020). It was found that the pressure dependence of Ni partitioning abruptly weakens at above 35 GPa, coinciding in pressure with the proposed conversion of four- to six-fold coordinated Si in molten basalt (Sanloup et al., 2013). However, with the additional data on Ni partitioning that have become available in the past decade, we find that the partition coefficient of Ni (D_{Ni}, open circles in Fig. 4) between metal and silicate evolves with pressure in a continuous fashion that lacks such kink. Note that D_{Ni} is controlled by the interplay of P, T, fO_2, and composition. When the effects of fO_2 and metal composition are taken into account, the calibrated partition coefficients (log K_{Ni}, solid circles in Fig. 4, details in SI) are much less scattered and the rather smooth curve indicates a continuous evolution of Ni partitioning with pressure. Furthermore, when corrected for temperature effect, Ni partitioning shows linear dependence on pressure up to at least 80 GPa (Fig. S7, details in SI), consistent with the gradual structural changes observed from velocity data and simulations on pyrolite.

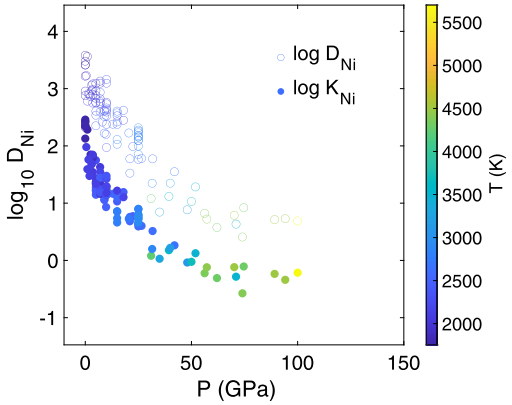

Fig. 4. Partitioning of Ni between metal and silicate melts as a function of pressure. D_{Ni} is calculated from the molar ratio $x_{Ni}^{metal}/x_{NiO}^{silicate}$ measured in the two phases, based on a compilation from previous studies (Hillgren et al., 1996; Jana and Walker, 1997; Gessmann and Rubie, 1998; Bouhifd and Jephcoat, 2003; Kegler et al., 2008; Bouhifd and Jephcoat, 2011; Siebert et al., 2011, 2012; Fischer et al., 2015; Huang and Badro, 2018). K_{Ni}, i.e. D_{Ni} corrected for metal composition and fO_2 effects, decreases gradually with increasing pressure and temperature, consistent with the gradual structural changes in melts (see main text).

The significance of smooth structural changes in pyrolite glass lies in the fact that it singles out the substantial effect of composi-

tion on melt structure/properties, which needs to be considered in magma ocean models. Among others, transport properties are fundamentally affected by compositional variations in silicate melts. For instance, viscosity (transport of momentum) was found to decrease in increasingly depolymerized silicate melts (e.g. (Lacks et al., 2007)), and in a pyrolitic basal magma ocean, the electrical conductivity can be sufficiently high to produce a silicate dynamo that might be responsible for the Archean magnetic field (Stixrude et al., 2020). In regard to density, our transverse wave velocity data distinguish pyrolite from SiO_2 glass. For pressure-induced changes are lacking discontinuity in the former, one would expect the density profile in a pyrolitic magma ocean to be the result of isochemical compression (cf. (Birch, 1952)), and any pressure-induced density anomaly unlikely, which is confirmed by our simulated densities for pyrolite melt (Fig. S8, Table S2). Should the density profile change smoothly with depth, it would facilitate an extremely turbulent convection in the whole magma ocean (Solomatov, 2000). Subsequently, as the first solids crystallize from the magma ocean, the fractionation between cumulates and residual melts commences.

CRediT authorship contribution statement

D.H. and M.M. designed research; D.H., M.M., C.M. and S.P. performed research; D.H., M.M., J.B. and S.P. analyzed data; D.H. wrote the paper with input from all authors.

Declaration of competing interest

The authors declare that they have no known competing financial interests or personal relationships that could have appeared to influence the work reported in this paper.

Acknowledgements

We are grateful to James Badro for help with glass synthesis; Julien Allaz for assistance with microprobe analysis; Thomas de Selva-Dewint for help with Brillouin experiments. We thank two anonymous reviewers for their constructive comments and Rajdeep Dasgupta for handling this manuscript. M.M. acknowledges support from the ETH startup funding. Simulations were performed using the ARCHER UK National Supercomputing Service.

Appendix A. Supplementary material

Supplementary material related to this article can be found online at https://doi.org/10.1016/j.epsl.2022.117473.

References

Akahama, Y., Kawamura, H., 2004. High-pressure Raman spectroscopy of diamond anvils to 250 GPa: method for pressure determination in the multimegabar pressure range. J. Appl. Phys. 96, 3748–3751. https://doi.org/10.1063/1.1778482.

Badro, J., Brodholt, J.P., Piet, H., Siebert, J., Ryerson, F.J., 2015. Core formation and core composition from coupled geochemical and geophysical constraints. Proc. Natl. Acad. Sci. USA 112, 12310. https://doi.org/10.1073/pnas.1505672112. http://www.pnas.org/content/112/40/12310.abstract.

Bajgain, S., Ghosh, D.B., Karki, B.B., 2015. Structure and density of basaltic melts at mantle conditions from first-principles simulations. Nat. Commun. 6, 8578. https://doi.org/10.1038/ncomms9578.

Benmore, C.J., Soignard, E., Amin, S.A., Guthrie, M., Shastri, S.D., Lee, P.L., Yarger, J.L., 2010. Structural and topological changes in silica glass at pressure. Phys. Rev. B 81, 054105. https://doi.org/10.1103/PhysRevB.81.054105.

Birch, F., 1952. Elasticity and constitution of the Earth's interior. J. Geophys. Res. 1896–1977 (57), 227–286. https://doi.org/10.1029/JZ057i002p00227.

Blöchl, P.E., 1994. Projector augmented-wave method. Phys. Rev. B 50, 17953–17979. https://doi.org/10.1103/PhysRevB.50.17953.

Bouhifd, M.A., Jephcoat, A.P., 2003. The effect of pressure on partitioning of Ni and Co between silicate and iron-rich metal liquids: a diamond-anvil cell study. Earth Planet. Sci. Lett. 209, 245–255. https://doi.org/10.1016/S0012-821X(03)00076-1.

Bouhifd, M.A., Jephcoat, A.P., 2011. Convergence of Ni and Co metal - silicate partition coefficients in the deep magma-ocean and coupled silicon - oxygen solubility in iron melts at high pressures. Earth Planet. Sci. Lett. 307, 341–348. https://doi.org/10.1016/j.epsl.2011.05.006.

Caracas, R., Hirose, K., Nomura, R., Ballmer, M.D., 2019. Melt - crystal density crossover in a deep magma ocean. Earth Planet. Sci. Lett. 516, 202–211. https://doi.org/10.1016/j.epsl.2019.03.031.

Elkins-Tanton, L.T., 2012. Magma oceans in the inner solar system. Annu. Rev. Earth Planet. Sci. 40, 113–139. https://doi.org/10.1146/annurev-earth-042711-105503.

Feng, S., Majumdar, A., Kuang, H., Pan, Y., Iitaka, T., Tse, J.S., 2021. A comparative study on pressure-induced structural transformations in a basaltic glass and melt from ab initio molecular dynamics calculations. Phys. Chem. Miner. 48, 41. https://doi.org/10.1007/s00269-021-01165-3.

Fischer, R.A., Nakajima, Y., Campbell, A.J., Frost, D.J., Harries, D., Langenhorst, F., Miyajima, N., Pollok, K., Rubie, D.C., 2015. High pressure metal-silicate partitioning of Ni, Co, V, Cr, Si, and O. Cosmochim. Acta 167, 177–194. https://doi.org/10.1016/j.gca.2015.06.026.

Gessmann, C.K., Rubie, D.C., 1998. The effect of temperature on the partitioning of nickel, cobalt, manganese, chromium, and vanadium at 9 GPa and constraints on formation of the Earth's core. Geochim. Cosmochim. Acta 62, 867–882. https://doi.org/10.1016/S0016-7037(98)00023-4.

Hillgren, V.J., Drake, M.J., Rubie, D.C., 1996. High pressure and high temperature metal-silicate partitioning of siderophile elements: the importance of silicate liquid composition. Geochim. Cosmochim. Acta 60, 2257–2263. https://doi.org/10.1016/0016-7037(96)00079-8.

Huang, D., Badro, J., 2018. Fe-Ni ideality during core formation on Earth. Am. Mineral. 103, 1701–1710. https://doi.org/10.2138/am-2018-6651.

Huang, D., Badro, J., Siebert, J., 2020. The niobium and tantalum concentration in the mantle constrains the composition of Earth's primordial magma ocean. Proc. Natl. Acad. Sci. 117, 27893–27898. https://doi.org/10.1073/pnas.2007982117. https://www.pnas.org/content/117/45/27893.

Jana, D., Walker, D., 1997. The influence of silicate melt composition on distribution of siderophile elements among metal and silicate liquids. Earth Planet. Sci. Lett. 150, 463–472. https://doi.org/10.1016/S0012-821X(97)00079-4. http://www.sciencedirect.com/science/article/pii/S0012821X97000794.

Karki, B.B., Bhattarai, D., Stixrude, L., 2007. First-principles simulations of liquid silica: structural and dynamical behavior at high pressure. Phys. Rev. B 76, 104205. https://doi.org/10.1103/PhysRevB.76.104205.

Karki, B.B., Stixrude, L.P., 2010. Viscosity of $MgSiO_3$ liquid at Earth's mantle conditions: implications for an early magma ocean. Science 328, 740–742. https://doi.org/10.1126/science.1188327.

Kegler, P., Holzheid, A., Frost, D.J., Rubie, D.C., Dohmen, R., Palme, H., 2008. New Ni and Co metal-silicate partitioning data and their relevance for an early terrestrial magma ocean. Earth Planet. Sci. Lett. 268, 28–40. https://doi.org/10.1016/j.epsl.2007.12.020.

Keppler, H., Rubie, D.C., 1993. Pressure-induced coordination changes of transition-metal ions in silicate melts. Nature 364, 54–56. https://doi.org/10.1038/364054a0.

Kim, Y.H., Yi, Y.S., Kim, H.I., Chow, P., Xiao, Y., Shen, G., Lee, S.K., 2019. Structural transitions in $MgSiO_3$ glasses and melts at the core-mantle boundary observed via inelastic X-ray scattering. Geophys. Res. Lett. 46, 13756–13764. https://doi.org/10.1029/2019GL085889.

Kono, Y., Shibazaki, Y., Kenney-Benson, C., Wang, Y., Shen, G., 2018. Pressure-induced structural change in $MgSiO_3$ glass at pressures near the Earth's core–mantle boundary. Proc. Natl. Acad. Sci. 115, 1742–1747. https://doi.org/10.1073/pnas.1716748115. https://www.pnas.org/content/115/8/1742.full.pdf.

Kono, Y., Shu, Y., Kenney-Benson, C., Wang, Y., Shen, G., 2020. Structural evolution of sio_2 glass with Si coordination number greater than 6. Phys. Rev. Lett. 125, 205701. https://doi.org/10.1103/PhysRevLett.125.205701.

Kresse, G., Hafner, J., 1993. Ab initio molecular dynamcis for liquid metals. Phys. Rev. B 47, 558. https://doi.org/10.1103/PhysRevB.47.558.

Kresse, G., Joubert, D., 1999. From ultrasoft pseudopotentials to the projector augmented-wave method. Phys. Rev. B, Condens. Matter Mater. Phys. 59, 1758–1775. https://doi.org/10.1103/PhysRevB.59.1758. http://prb.aps.org/abstract/PRB/v59/i3/p1758_1.

Lacks, D.J., Rear, D.B., Van Orman, J.A., 2007. Molecular dynamics investigation of viscosity, chemical diffusivities and partial molar volumes of liquids along the $Mgo–SiO_2$ join as functions of pressure. Geochim. Cosmochim. Acta 71, 1312–1323. https://doi.org/10.1016/j.gca.2006.11.030. https://www.sciencedirect.com/science/article/pii/S0016703706022174.

Lee, S.K., Lin, J.F., Cai, Y.Q., Hiraoka, N., Eng, P.J., Okuchi, T., Mao, H.k., Meng, Y., Hu, M.Y., Chow, P., Shu, J., Li, B., Fukui, H., Lee, B.H., Kim, H.N., Yoo, C.S., 2008. X-ray Raman scattering study of $MgSiO_3$ glass at high pressure: implication for triclustered $MgSiO_3$ melt in Earth's mantle. Proc. Natl. Acad. Sci. 105, 7925–7929. https://doi.org/10.1073/pnas.0802667105. https://www.pnas.org/content/105/23/7925.full.pdf.

Li, J., Agee, C.B., 1996. Geochemistry of mantle-core differentiation at high pressure. Nature 381, 686–689. https://doi.org/10.1038/381686a0.

Maeda, F., Kamada, S., Ohtani, E., Hirao, N., Mitsui, T., Masuda, R., Miyahara, M., McCammon, C., 2017. Spin state and electronic environment of iron in basaltic glass

in the lower mantle. Am. Mineral. 102, 2106–2112. https://doi.org/10.2138/am-2017-6035.

Majumdar, A., Wu, M., Pan, Y., Iitaka, T., Tse, J.S., 2020. Structural dynamics of basaltic melt at mantle conditions with implications for magma oceans and superplumes. Nat. Commun. 11, 4815. https://doi.org/10.1038/s41467-020-18660-w.

McDonough, W., Sun, S.s., 1995. The composition of the Earth. Chem. Geol. 120, 223–253. https://doi.org/10.1016/0009-2541(94)00140-4. http://www.sciencedirect.com/science/article/pii/0009254194001404.

Murakami, M., Bass, J.D., 2010. Spectroscopic evidence for ultrahigh-pressure polymorphism in SiO_2 glass. Phys. Rev. Lett. 104, 025504. https://doi.org/10.1103/PhysRevLett.104.025504.

Murakami, M., Bass, J.D., 2011. Evidence of denser $MgSiO_3$ glass above 133 gigapascal (GPa) and implications for remnants of ultradense silicate melt from a deep magma ocean. Proc. Natl. Acad. Sci. 108, 17286–17289. https://doi.org/10.1073/pnas.1109748108. https://www.pnas.org/content/108/42/17286.full.pdf.

Mysen, B., 1983. The structure of silicate melts. Annu. Rev. Earth Planet. Sci. 11, 75–97. https://doi.org/10.1248/cpb.10.879.

Nomura, R., Ozawa, H., Tateno, S., Hirose, K., Hernlund, J., Muto, S., Ishii, H., Hiraoka, N., 2011. Spin crossover and iron-rich silicate melt in the Earth's deep mantle. Nature 473, 199–202. https://doi.org/10.1038/nature09940.

Perdew, J.P., Burke, K., Ernzerhof, M., 1996. Generalized gradient approximation made simple. Phys. Rev. Lett. 77, 3865–3868. https://doi.org/10.1103/PhysRevLett.77.3865.

Petitgirard, S., Malfait, W.J., Journaux, B., Collings, I.E., Jennings, E.S., Blanchard, I., Kantor, I., Kurnosov, A., Cotte, M., Dane, T., Burghammer, M., Rubie, D.C., 2017. SiO_2 glass density to lower-mantle pressures. Phys. Rev. Lett. 119, 215701. https://doi.org/10.1103/PhysRevLett.119.215701.

Petitgirard, S., Malfait, W.J., Sinmyo, R., Kupenko, I., Hennet, L., Harries, D., Dane, T., Burghammer, M., Rubie, D.C., 2015. Fate of $MgSiO_3$ melts at core-mantle boundary conditions. Proc. Natl. Acad. Sci. USA 112, 14186. https://doi.org/10.1073/pnas.1512386112. http://www.pnas.org/content/112/46/14186.abstract.

Petitgirard, S., Sahle, C.J., Weis, C., Gilmore, K., Spiekermann, G., Tse, J.S., Wilke, M., Cavallari, C., Cerantola, V., Sternemann, C., 2019. Magma properties at deep Earth's conditions from electronic structure of silica. Geochem. Perspect. Lett. 9, 32–37. https://doi.org/10.7185/geochemlet.1902. http://www.geochemicalperspectivesletters.org/article1902.

Prescher, C., Prakapenka, V.B., Stefanski, J., Jahn, S., Skinner, L.B., Wang, Y., 2017. Beyond sixfold coordinated Si in SiO_2 glass at ultrahigh pressures. Proc. Natl. Acad. Sci. 114, 10041–10046. https://doi.org/10.1073/pnas.1708882114. https://www.pnas.org/content/114/38/10041.full.pdf.

Sanchez-Valle, C., Bass, J.D., 2010. Elasticity and pressure-induced structural changes in vitreous $MgSiO_3$-enstatite to lower mantle pressures. Earth Planet. Sci. Lett. 295, 523–530. https://doi.org/10.1016/j.epsl.2010.04.034. https://www.sciencedirect.com/science/article/pii/S0012821X10002803.

Sanloup, C., Drewitt, J.W.E., Konôpková, Z., Dalladay-Simpson, P., Morton, D.M., Rai, N., Van Westrenen, W., Morgenroth, W., 2013. Structural change in molten basalt at deep mantle conditions. Nature 503, 104–107. https://doi.org/10.1038/nature12668.

Sato, T., Funamori, N., 2010. High-pressure structural transformation of SiO_2 glass up to 100 GPa. Phys. Rev. B 82, 184102. https://doi.org/10.1103/PhysRevB.82.184102.

Siebert, J., Badro, J., Antonangeli, D., Ryerson, F.J., 2012. Metal-silicate partitioning of Ni and Co in a deep magma ocean. Earth Planet. Sci. Lett. 321–322, 189–197. https://doi.org/10.1016/j.epsl.2012.01.013.

Siebert, J., Corgne, A., Ryerson, F.J., 2011. Systematics of metal-silicate partitioning for many siderophile elements applied to Earth's core formation. Geochim. Cosmochim. Acta 75, 1451–1489. https://doi.org/10.1016/j.gca.2010.12.013.

Solomatov, V., 2015. 9.04 - magma oceans and primordial mantle differentiation. In: Schubert, G. (Ed.), Treatise on Geophysics, second edition. Elsevier, Oxford, pp. 81–104. https://www.sciencedirect.com/science/article/pii/B978044453802400155X.

Solomatov, V.S., 2000. Fluid Dynamics of a Terrestrial Magma Ocean, pp. 323–338.

Solomatova, N.V., Caracas, R., 2019. Pressure-induced coordination changes in a pyrolitic silicate melt from ab initio molecular dynamics simulations. J. Geophys. Res., Solid Earth 124, 11232–11250. https://doi.org/10.1029/2019JB018238.

Spera, F.J., Ghiorso, M.S., Nevins, D., 2011. Structure, thermodynamic and transport properties of liquid $MgSiO_3$: comparison of molecular models and laboratory results. Geochim. Cosmochim. Acta 75, 1272–1296. https://doi.org/10.1016/j.gca.2010.12.004. https://www.sciencedirect.com/science/article/pii/S0016703710006678.

Stixrude, L., Karki, B., 2005. Structure and freezing of $MgSiO_3$ liquid in Earth's lower mantle. Science 310, 297–299. https://doi.org/10.1126/science.1116952. https://www.sciencemag.org/lookup/doi/10.1126/science.1116952.

Stixrude, L., Scipioni, R., Desjarlais, M.P., 2020. A silicate dynamo in the early Earth. Nat. Commun. 11, 935. https://doi.org/10.1038/s41467-020-14773-4.

Takahashi, E., 1986. Melting of a dry peridotite KLB-1 up to 14 GPa: implications on the origin of peridotitic upper mantle. J. Geophys. Res. 91, 9367. https://doi.org/10.1029/JB091iB09p09367.